Editors' Suggestion | Featured in Physics

3D Dirac Plasmons in the Type-II Dirac Semimetal $PtTe_2$

Antonio Politano,[1,*] Gennaro Chiarello,[2,†] Barun Ghosh,[3] Krishanu Sadhukhan,[3] Chia-Nung Kuo,[4] Chin Shan Lue,[4] Vittorio Pellegrini,[1] and Amit Agarwal[3,‡]

[1]*Istituto Italiano di Tecnologia-Graphene Labs via Morego, 30 16163 Genova, Italy*
[2]*Department of Physics, University of Calabria, via ponte Bucci, cubo 31/C 87036, Rende (CS), Italy*
[3]*Department of Physics, Indian Institute of Technology Kanpur, Kanpur—208016, India*
[4]*Department of Physics, National Cheng Kung University, 1 Ta-Hsueh Road 70101 Tainan, Taiwan*

(Received 4 March 2018; published 22 August 2018)

Transition-metal dichalcogenides showing type-II Dirac fermions are emerging as innovative materials for nanoelectronics. However, their excitation spectrum is mostly unexplored yet. By means of high-resolution electron energy loss spectroscopy and density functional theory, here, we identify the collective excitations of type-II Dirac fermions (3D Dirac plasmons) in $PtTe_2$ single crystals. The observed plasmon energy in the long-wavelength limit is ∼0.5 eV, which makes $PtTe_2$ suitable for near-infrared optoelectronic applications. We also demonstrate that interband transitions between the two Dirac bands in $PtTe_2$ give rise to additional excitations at ∼1 and ∼1.4 eV. Our results are crucial to bringing to fruition type-II Dirac semimetals in optoelectronics.

DOI: 10.1103/PhysRevLett.121.086804

Recently, topological Dirac semimetals (DSMs) have attracted considerable interest [1–3]. In DSM systems, Dirac fermions are present in three-dimensional (3D) samples, without the experimental complication of implementing a single layer, as in the case of graphene. In DSMs, doubly degenerate conduction and valence bands cross linearly at Dirac points. The electronic dispersion relation of the low-energy excitations around these points is linear and resembles the massless Dirac equation of relativistic particle physics.

The electronic dispersion of a Dirac semimetal $E_{\mathbf{k}}$ can be expressed as $E_{\mathbf{k}} = U_{\mathbf{k}} \pm T_{\mathbf{k}}$, with $U_{\mathbf{k}}$ and $T_{\mathbf{k}}$ being analogous to the potential and kinetic energy components, respectively. $U_{\mathbf{k}}$ gives a tilt to the Dirac-cone dispersion. For a given $\mathbf{k}$ direction, if $U_{\mathbf{k}} > T_{\mathbf{k}}$, then the Dirac cone appears to be "tilted-over" in that direction, and the system is called a type-II Dirac semimetal, as opposed to an ordinary type-I Dirac semimetal. In a type-I Dirac semimetal, such as Na_3Bi and Cd_3As_2 [1,4–6], the Fermi surface at the Dirac point is an isolated point. Just above (below) the Dirac point, the Fermi surface encloses a closed region of electrons (holes). Additionally, the two crossing bands have the opposite sign of the Fermi velocity throughout the Brillouin zone. Conversely, in a Lorentz-symmetry violating type-II Dirac semimetal [7,8], the Dirac point occurs at the intersection of an electron and a hole pocket, on account of the tilted-over nature of the Dirac-cone dispersion. In these systems, the crossing bands have the same sign as the Fermi velocity in certain directions. This enables novel physical properties, such as anisotropic magnetotransport [7,8].

Recently, type-II Dirac fermions have been predicted for PtX_2 (X = S, Se, Te) [9] and $PdTe_2$ [10] transition-metal dichalcogenides (TMDCs), YPd_2Sn [11], VAl_3 [12], and graphynelike photonic lattices [13]. Experimentally, type-II Dirac fermions have been found in $PtTe_2$ [14,15], $PtSe_2$ [16], and $PdTe_2$ [15,17] by angle-resolved photoemission spectroscopy (ARPES) experiments reporting anisotropic and tilted Dirac cones. The high electron mobility in this class of TMDCs at room temperature also enables the fabrication of field-effect transistors with potential applications in optoelectronics [18–20], even though their excitation spectrum is unexplored.

In the prospect of plasmonic devices based on 3D Dirac fermions, the possibility of using a few layers exfoliated from a parental layered bulk crystal as active channels in nanodevices [21] is crucial. Unfortunately, $PtSe_2$ fails to fulfil this prerequisite (see Sec. S1 in the Supplemental Material (SM) [22] for more details). By contrast, $PtTe_2$ can be grown as bulk crystals with superb crystalline quality and it can be easily exfoliated.

Here, we provide direct evidence of the existence of 3D Dirac plasmons in the excitation spectrum of DSM $PtTe_2$ by means of high-resolution electron energy loss spectroscopy (HREELS) and density functional theory (DFT), complemented by effective low-energy theory calculations. We observe a gapped intraband Dirac plasmon at ∼0.5 eV in the long-wavelength limit, in addition to two other excitations at ∼1 and ∼1.4 eV, which predominantly originate from direct transitions between the two bands hosting Dirac quasiparticles.

Single crystals of $PtTe_2$ were prepared by the self-flux method. Their structure was examined by x-ray diffraction (Fig. S1 of the SM [22]). Freshly cleaved samples were characterized *in situ* via a combination of surface-science

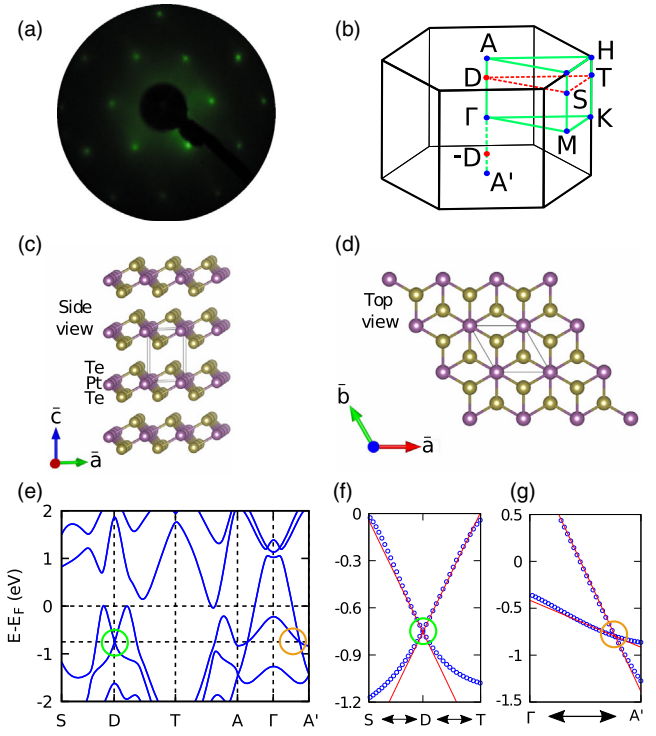

FIG. 1. (a) The LEED pattern of (0001)-oriented $PtTe_2$ single crystals, acquired at a primary electron beam energy of 74 eV. (b) Brillouin zone of $PtTe_2$. The two Dirac points are located on the $A-\Gamma-A'$ line at $\pm D$. (c) and (d) show the side and top views of the crystal structure, respectively. The purple and yellow balls denote the Pt and Te atoms, respectively. (e) The band structure of $PtTe_2$, showing the two Dirac points tilted in opposite directions, located on the $A-\Gamma-A'$ axis. The dispersion around each of the Dirac points is isotropic in the horizontal *SDT* plane (parallel to the experimental ΓKM plane) and anisotropic and "tilted" along the $\Gamma-A$ direction. A magnification of the band structure around one of the Dirac points, along with the fit of the low-energy dispersion [see Eq. (1)], is shown in panels (f) for the isotropic *SDT* direction [marked by the green circle in (e)], and along the $\Gamma-A'$ direction in (g) [marked by the orange circle in (e)].

techniques (see Sec. S4 in the SM [22]). The surface exhibited an excellent (1×1) hexagonal low-energy electron diffraction (LEED) pattern [see Fig. 1(a)]. X-ray photoelectron spectroscopy (Fig. S2 in the SM [22]) and vibrational experiments (Fig. S3 in the SM [22]) demonstrate the absence of any surface contamination and chemical inertness.

$PtTe_2$ crystallizes in the trigonal CdI_2-type crystal structure (see Fig. 1), space group $P\bar{3}m1$ (No. 164). Each Pt atom is surrounded by six Te atoms, forming $PtTe_6$ octahedra along the basal plane. The octahedra link at their edges to form infinite sheets. The Brillouin zone and the crystal structure are shown in Figs. 1(b)–1(d), respectively. The band structure, calculated using the generalized gradient approximation (GGA) for the exchange-correlation functional in DFT, is shown in Fig. 1(e). The two Dirac points appear on the $A-\Gamma-A'$ axis at $\pm D=\{0,0,\pm k_z^{\mathrm{D}}\}$, with $k_z^{\mathrm{D}}=0.37\times2\pi/c$. By virtue of the inversion symmetry about the Γ point, the electronic dispersion around the two Dirac points at $\pm D$ are tilted in opposite directions, as also indicated by Eq. (1) below. Both these Dirac points at $\pm D$ appear at an energy $E_D=-0.76$ eV, below the chemical potential μ. The band structure, as well as the occurrence of two oppositely tilted Dirac points, are validated qualitatively by comparison with available ARPES measurements [14,15].

In the vicinity of the two Dirac points, the effective low-energy Hamiltonian for bulk $PtTe_2$, which describes an anisotropic and tilted 3D Dirac cone, is given by [9]

$$\mathcal{H}_\chi=\hbar(\chi v_t k_z\sigma_0+v_x k_x\sigma_x-v_y k_y\sigma_y-\chi v_z k_z\sigma_z). \quad (1)$$

Here, $\chi=\pm1$ denotes the two Dirac cones centered at $\mp D$ with the tilt in the opposite direction, σ_0 is the 2×2 identity matrix and σ_i's are the Pauli spin matrices. The corresponding energy dispersion is given by $\varepsilon^{\chi}_{\lambda\mathbf{k}}=\chi\hbar v_t k_z+\lambda\hbar\sqrt{v_x^2k_x^2+v_y^2k_y^2+v_z^2k_z^2}$, where the band index $\lambda=+1(-1)$ denotes the conduction (valence) band. The low-energy fit based on Eq. (1) to the GGA-DFT band-structure is shown in Figs. 1(f) and 1(g) and the corresponding velocities are found to be $\{v_x,v_y,v_z,v_t\}=\{0.65,0.65,0.35,0.51\}\times10^6$ m/s.

Dispersion of the loss peaks in HREELS, i.e., $E_{\mathrm{loss}}(q)$, was measured by moving the analyzer, while keeping the sample and the monochromator in a fixed position. Specifically, the experimental setup for angle-resolved HREELS experiments shown in Fig. 2(a) has been chosen in order to selectively probe wave vector transfer (calculated following Ref. [56]) along the $\Gamma-K$ direction.

Figure 2(a) shows the excitation spectrum probed by HREELS with primary electron beam energy $E_p=6$ eV for different values of the scattering angle. These experimental conditions are optimal for probing bulk excitations (see Sec. S9 of the SM [22] for more details). We observe a single peak, whose energy shifts with the scattering angle from ~0.5 up to ~0.7 eV. We assign this feature to a 3D Dirac plasmonic mode. The corresponding dispersion relation of the plasmon frequency as a function of the wave vector is represented by the green circles in Fig. 2(b). The possibility that the observed mode could be a Dirac hyperbolic polariton [57] can be unambiguously ruled out. In fact, composite modes arising from the hybridization of phonon modes with Dirac plasmons (previously observed by our group in graphene [58]) should have a gap of the order of the highest branch of optical phonons in $PtTe_2$, i.e., 0.02 eV (see Sec. S9 of the SM [22]), which is significantly smaller than the observed gap.

To establish the connection of the observed plasmonic excitation with Dirac-cone electrons, we analytically calculate the anisotropic noninteracting (NI) density-density response function $\Pi^{\mathrm{NI}}(\mathbf{q},\omega)$ for the effective

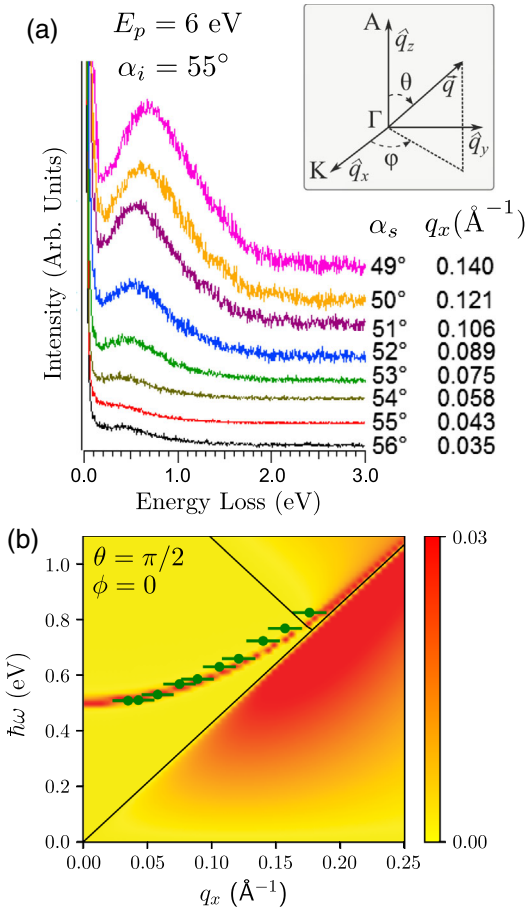

FIG. 2. (a) Wave-vector-resolved HREELS spectra, acquired for $E_p = 6$ eV as a function of the scattering angle. The corresponding value of the wave vector along the $\Gamma - K$ direction (or along $\hat{q}_x$ with $\theta = \pi/2$ and $\phi = 0$, as indicated in the inset) is reported on the right. All HREELS experiments have been carried out at room temperature. (b) The experimentally measured Dirac-plasmon dispersion is indicated with green circles, along with the theoretically calculated loss function for $PtTe_2$ [see Eq. (2)], in the $\Gamma - K$ direction (with $\theta = \pi/2$ and $\phi = 0$). The green bars indicate the experimental inaccuracy in determining q (see Sec. S3 in the SM [22] for its evaluation). The $\mathcal{E}_{\text{Loss}}$ is calculated using the low-energy tilted and anisotropic Dirac Hamiltonian in Eq. (1). The yellow (red) region bounded by the black lines indicates the absence (presence) of single-particle excitations in the $\omega - q$ plane. The plasmon enters the interband single-particle excitation regime for $q > 0.17$ Å^{-1} and becomes increasingly damped.

low-energy Hamiltonian in Eq. (1). Within the random-phase approximation (RPA), the interacting density-density response function is given by $\Pi^{\text{RPA}}(\mathbf{q},\omega) = \Pi^{\text{NI}}(\mathbf{q},\omega)/\epsilon^{\text{RPA}}(\mathbf{q},\omega)$, where $\epsilon^{\text{RPA}}(\mathbf{q},\omega) = 1 - v_q \Pi^{\text{NI}}(\mathbf{q},\omega)$ is the dynamical dielectric function. Here, $v_q = 4\pi e^2/\kappa q^2$ is the Coulomb interaction in the Fourier space in 3D, with κ denoting the dielectric constant. Within RPA, the frequency of the bulk plasmon mode is given by the zeros of the dynamical dielectric function: $\epsilon^{\text{RPA}}(\mathbf{q},\omega) = 0$ [59]. Plasmons appear as peaks in the electron energy loss function defined by

$$\mathcal{E}_{\text{loss}} = -\Im m\left(\frac{1}{\epsilon^{\text{RPA}}}\right), \tag{2}$$

which is proportional to the experimental excitation spectrum probed by HREELS. The full analytical expression of the anisotropic density-density response function is presented in Sec. S7 of the SM [22].

In the long-wavelength limit, the plasmon gap at $q = 0$ ($\hbar\omega_{\text{pl}} \to \Delta_{\text{pl}}$) is given by the self-consistent solution of the transcendental equation

$$\Delta_{\text{pl}} = \mu f(\theta,\phi)\sqrt{\frac{4g\alpha_{\text{fine}}}{3\pi[1 + 2\gamma(\Delta_{\text{pl}})]}}, \tag{3}$$

where $\alpha_{\text{fine}} = e^2 v_x/(\kappa\hbar v_z v_y)$ is the effective fine structure constant. In Eq. (3), we have defined

$$\gamma(\varepsilon) = \frac{g\alpha_{\text{fine}} f^2(\theta,\phi)}{6\pi}\log\left|\frac{4\varepsilon_{\text{max}}^2}{4\mu^2 - \varepsilon^2}\right|, \tag{4}$$

with ε_{max} denoting the high-energy cutoff of the Dirac bands and $f^2(\theta,\phi) = \sin^2\theta(\cos^2\phi + v_y^2\sin^2\phi/v_x^2) + v_z^2\cos^2\theta/v_x^2$. Here, θ and ϕ denote the polar and azimuthal angle of the $\mathbf{q}$ vector, as shown in the inset to Fig. 2(a). Interestingly, in 3D the anisotropy of the band structure makes the plasmon gap direction dependent; i.e., it depends on how the long-wavelength $q \to 0$ limit is approached (see Fig. S8 in the SM [22] for details). This is in contrast to 2D systems, for which the plasmon mode is gapless and the anisotropy of the band structure only reflects in the anisotropic plasmon dispersion [60,61].

In the limiting case of weak Coulomb interactions —$\kappa \to \infty$, or $\alpha_{\text{fine}} \ll 1$ limit—we have $\gamma(\varepsilon) \to 0$, and, to lowest order in α_{fine}, the anisotropic plasmon gap reduces to

$$\Delta_{\text{pl}} \to \Delta_{\text{pl}}^{(0)} \equiv \mu f(\theta,\phi)\sqrt{\frac{4g\alpha_{\text{fine}}}{3\pi}}, \tag{5}$$

which is completely independent of ε_{max}. However, $\Delta_{\text{pl}}^{(0)}$ generally denotes the upper limit of the plasmon gap. The actual plasmon gap Δ_{pl} depends on the cutoff energy if $\alpha_{\text{fine}} \geq 1$ and it decreases monotonically with reducing cutoff (see Fig. S9 of the SM [22] for details). Note that, in Eq. (3), we have $\Delta_{\text{pl}} \propto \mu$, and, since in 3D massless Dirac systems $\mu \propto n^{1/3}$ (where n denotes the carrier density), $\Delta_{\text{pl}} \propto n^{1/3}$ [62].

Figure 2(b) shows the loss function calculated analytically within RPA [see Eq. (2)], using the low-energy effective Hamiltonian for the two tilted and anisotropic Dirac cones, as specified in Eq. (1). Here, we have chosen the chemical potential $\mu = -E_D = 0.76$ eV, $\kappa = 1$, and the

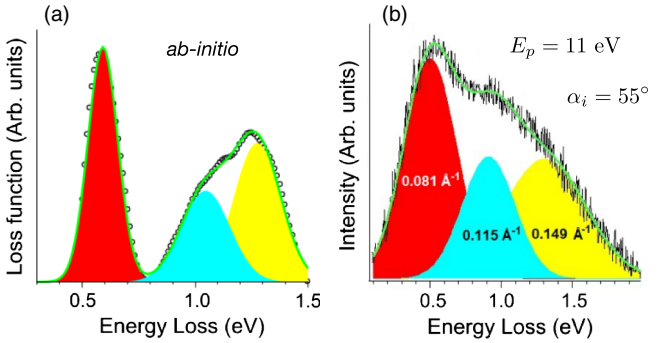

FIG. 3. (a) *Ab initio* loss function for the selected case of $q = 0.026$ Å^{-1} along the $\Gamma - K$ direction. The colored region enclosed by the green curve shows a fit with three Gaussian line shapes to the DFT-based loss function (in black circles). (b) HREELS spectrum recorded for a higher value of impinging energy ($E_p = 11$ eV), enabling the observation of three well-separated spectral components. In both theoretical and experimental loss functions, background has been subtracted.

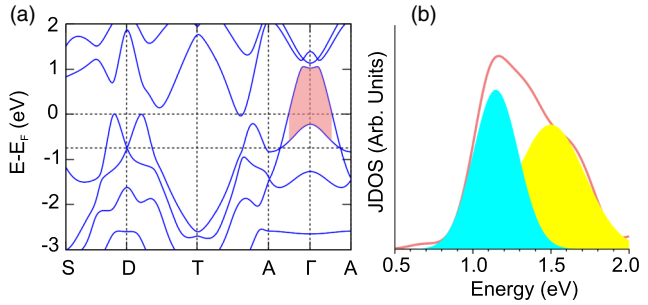

FIG. 4. The direct transitions between the two bands hosting Dirac Fermions, for $\mu = -E_D = 0.76$ eV above the Dirac points, shaded by pink in panel (a), give rise to the joint density of states (JDOS) shown in (b). The JDOS under the pink curve in (b) can be resolved as a sum of two Gaussians of roughly equal strength, with one of them centered around ∼1 eV and the other around ∼1.5 eV. The two JDOS peaks are consistent with the additional peaks resolved in the excitation spectrum experimentally probed by HREELS with higher impinging energies [see Fig. 3(b)].

energy cutoff has been tuned to make the theoretical results consistent with the experimentally measured plasmon frequency for the lowest wave vector. Overall, we note a good agreement of the theoretical dispersion relation with the experimental curve (denoted by green circles in Fig. 2) [63]. Note that the plasmon enters the continuum of the interband single-particle excitations for $q > 0.17$ Å^{-1}.

Going beyond the effective low-energy theory, we calculate the *ab initio* based loss function, shown in Fig. 3(a) (see Sec. S9 of the SM [22] for details of the calculations). In addition to the 3D Dirac-plasmon peak, we also find additional modes at ∼1 and ∼1.4 eV. To check their existence experimentally, it is mandatory to increase E_p in order to reach a sufficient cross section for their excitation. Congruent with the predictions, the excitation spectrum probed by HREELS at $E_p = 11$ eV, shown in Fig. 3(b), exhibits two peaks around ∼1 and ∼1.4 eV, in addition to the 3D Dirac plasmon peak at ∼0.5 eV.

To understand the origin of the two additional features in the excitation spectrum at ∼1 and ∼1.4 eV, we calculate the joint density of states (JDOS) between different pairs of bands around the Fermi energy: $\rho_{ij}^{\mathrm{JDOS}}(E) = \sum_{\mathbf{k}} \delta(E_{\mathbf{k},i} - E_{\mathbf{k},j} - E)$, where i indicates an empty (or partially empty), and j a filled (or partially filled) band with $E_{\mathbf{k},i} > E_{\mathbf{k},j}$. The corresponding $\rho_{ij}^{\mathrm{JDOS}}(E)$ associated with the transitions between the two bands hosting the Dirac quasiparticles, for $\mu = -E_{\mathrm{D}} = 0.76$ eV above the two Dirac points, as highlighted by the shaded pink region in Fig. 4(a), is shown in Fig. 4(b). The resulting JDOS spectrum can be resolved into two Gaussian peaks, centered in the vicinity of ∼1 and ∼1.5 eV, broadly in agreement with the observed peaks in the HREELS spectrum. Therefore, we can affirm that the excitations at ∼1 and ∼1.4 eV in the loss function are predominantly originated by direct transitions between two 3D Dirac bands.

Another peculiarity of 3D Dirac plasmons is their robustness against surface modifications. As demonstrated in Ref. [64], 3D Dirac points in DSMs are protected by crystal symmetry and are robust against perturbations. In $PtTe_2$, the bulk space group $P\bar{3}m1$ has a threefold rotation symmetry, which stabilizes the Dirac cone. Correspondingly, 3D Dirac plasmons are also robust against surface modifications, due to their bulk nature. The robustness of 3D Dirac plasmons is notably beneficial in the prospect of possible DSM-based plasmonic applications. On the contrary, the Dirac plasmons in topological insulators and epitaxial graphene have been shown to be impacted significantly by surface degradation, since their origin lies in the surface states, which disappear upon surface oxidation (see Fig. S4 in the SM [22]).

In conclusion, we provided direct evidence of the existence of 3D Dirac plasmons in $PtTe_2$ with a gap of ∼0.5 eV. Moreover, we show that direct interband transitions between the two bands hosting the Dirac quasiparticles originate two additional peaks at ∼1 and ∼1.4 eV. Our results offer useful insights regarding the dielectric properties of type-II DSMs. The comprehension of their excitation spectrum is crucial for the promising prospect of plasmonic devices based on $PtTe_2$ single crystals, which are also cleavable, due to the weak van der Waals interlayer bonds, with subsequent ease for the nanofabrication process. Accordingly, this study helps to bring to fruition this class of materials in the semiunexplored field of DSM-based plasmonics.

We thank Vito Fabio for technical support in HREELS experiments. A. A. acknowledges funding from INSPIRE Faculty Grant No. IFA-12-PH14, by the Department of

Science and Technology, Government of India. B. G. thanks the Council of Industrial Research (CSIR)—India, for the Junior Research Fellowship.

*antonio.politano@iit.it
†gennaro.chiarello@fis.unical.it
‡amitag@iitk.ac.in

[1] Z. K. Liu, B. Zhou, Y. Zhang, Z. J. Wang, H. M. Weng, D. Prabhakaran, S.-K. Mo, Z. X. Shen, Z. Fang, X. Dai, Z. Hussain, and Y. L. Chen, Science **343**, 864 (2014).
[2] T. Schumann, L. Galletti, D. A. Kealhofer, H. Kim, M. Goyal, and S. Stemmer, Phys. Rev. Lett. **120**, 016801 (2018).
[3] A. A. Burkov, Phys. Rev. Lett. **120**, 016603 (2018).
[4] Z. Wang, H. Weng, Q. Wu, X. Dai, and Z. Fang, Phys. Rev. B **88**, 125427 (2013).
[5] Z. K. Liu, J. Jiang, B. Zhou, Z. J. Wang, Y. Zhang, H. M. Weng, D. Prabhakaran, S.-K. Mo, H. Peng, P. Dudin, T. Kim, M. Hoesch, Z. Fang, X. Dai, Z. X. Shen, D. L. Feng, Z. Hussain, and Y. L. Chen, Nat Mater. **13**, 677 (2014).
[6] Z. Wang, Y. Sun, X.-Q. Chen, C. Franchini, G. Xu, H. Weng, X. Dai, and Z. Fang, Phys. Rev. B **85**, 195320 (2012).
[7] G. Sharma, P. Goswami, and S. Tewari, Phys. Rev. B **96**, 045112 (2017).
[8] T. Liang, Q. Gibson, M. N. Ali, M. Liu, R. J. Cava, and N. P. Ong, Nat. Mater. **14**, 280 (2015).
[9] H. Huang, S. Zhou, and W. Duan, Phys. Rev. B **94**, 121117 (2016).
[10] F. Fei, X. Bo, R. Wang, B. Wu, J. Jiang, D. Fu, M. Gao, H. Zheng, Y. Chen, X. Wang, H. Bu, F. Song, X. Wan, B. Wang, and G. Wang, Phys. Rev. B **96**, 041201 (2017).
[11] P.-J. Guo, H.-C. Yang, K. Liu, and Z.-Y. Lu, Phys. Rev. B **95**, 155112 (2017).
[12] T.-R. Chang, S.-Y. Xu, D. S. Sanchez, W.-F. Tsai, S.-M. Huang, G. Chang, C.-H. Hsu, G. Bian, I. Belopolski, Z.-M. Yu, S. A. Yang, T. Neupert, H.-T. Jeng, H. Lin, and M. Z. Hasan, Phys. Rev. Lett. **119**, 026404 (2017).
[13] G. G. Pyrialakos, N. S. Nye, N. V. Kantartzis, and D. N. Christodoulides, Phys. Rev. Lett. **119**, 113901 (2017).
[14] M. Yan, H. Huang, K. Zhang, E. Wang, W. Yao, K. Deng, G. Wan, H. Zhang, M. Arita, H. Yang, Z. Sun, H. Yao, Y. Wu, S. Fan, W. Duan, and S. Zhou, Nat. Commun. **8**, 257 (2017).
[15] M. S. Bahramy *et al.*, Nat. Mater. **17**, 21 (2017).
[16] K. Zhang, M. Yan, H. Zhang, H. Huang, M. Arita, Z. Sun, W. Duan, Y. Wu, and S. Zhou, Phys. Rev. B **96**, 125102 (2017).
[17] H.-J. Noh, J. Jeong, E.-J. Cho, K. Kim, B. I. Min, and B.-G. Park, Phys. Rev. Lett. **119**, 016401 (2017).
[18] Y. Zhao, J. Qiao, Z. Yu, P. Yu, K. Xu, S. P. Lau, W. Zhou, Z. Liu, X. Wang, W. Ji, and Y. Chai, Adv. Mater. **29**, 1604230 (2017).
[19] Z. Wang, Q. Li, F. Besenbacher, and M. Dong, Adv. Mater. **28**, 10224 (2016).
[20] C. Yim, K. Lee, N. McEvoy, M. OBrien, S. Riazimehr, N. C. Berner, C. P. Cullen, J. Kotakoski, J. C. Meyer, M. C. Lemme *et al.*, ACS Nano **10**, 9550 (2016).
[21] G. Fiori, F. Bonaccorso, G. Iannaccone, T. Palacios, D. Neumaier, A. Seabaugh, S. K. Banerjee, and L. Colombo, Nat. Nanotechnol. **9**, 768 (2014).
[22] See Supplemental Material at http://link.aps.org/supplemental/10.1103/PhysRevLett.121.086804 for additional information on (i) experimental methods, (ii) quenching of Dirac plasmons in topological insulators and graphene, (iii) polarization and loss function calculation of an anisotropic and tilted Dirac cone based on low-energy theory, and (iv) *ab initio* calculations of the electronic band structure and the energy loss function, which includes Refs. [23–55].
[23] A. Politano, G. Chiarello, C.-N. Kuo, C. S. Lue, R. Edla, P. Torelli, V. Pellegrini, and D. W. Boukhvalov, Adv. Funct. Mater. **28**, 1706504 (2018).
[24] K. W. Richter and H. Ipser, J. Phase Equilib. **15**, 165 (1994).
[25] Y. Wang *et al.*, Nano Lett. **15**, 4013 (2015).
[26] A. Politano, V. M. Silkin, I. A. Nechaev, M. S. Vitiello, L. Viti, Z. S. Aliev, M. B. Babanly, G. Chiarello, P. M. Echenique, and E. V. Chulkov, Phys. Rev. Lett. **115**, 216802 (2015).
[27] A. Politano, G. J. Slotman, R. Roldn, G. Chiarello, D. Campi, M. I. Katsnelson, and S. Yuan, 2D Mater. **4**, 021001 (2017).
[28] A. Politano, M. Caputo, S. Nappini, F. Bondino, E. Magnano, Z. S. Aliev, M. B. Babanly, A. Goldoni, G. Chiarello, and E. V. Chulkov, J. Phys. Chem. C **118**, 21517 (2014).
[29] A. Politano, M. Cattelan, D. W. Boukhvalov, D. Campi, A. Cupolillo, S. Agnoli, N. G. Apostol, P. Lacovig, S. Lizzit, D. Farías, G. Chiarello, G. Granozzi, and R. Larciprete, ACS Nano **10**, 4543 (2016).
[30] A. Politano and G. Chiarello, Carbon **61**, 412 (2013).
[31] A. Politano, A. R. Marino, V. Formoso, and G. Chiarello, AIP Adv. **1**, 042130 (2011).
[32] W. M. Lau, L. J. Huang, I. Bello, Y. M. Yiu, and S. Lee, J. Appl. Phys. **75**, 3385 (1994).
[33] Y. Osetsky, A. Calder, and R. Stoller, Curr. Opin. Solid State Mater. Sci. **19**, 277 (2015).
[34] Z. Bastl, I. Spirovová, and M. Janovská, Collect. Czech. Chem. Commun. **62**, 199 (1997).
[35] D. Maccariello, A. Al Taleb, F. Calleja, A. L. Vzquez de Parga, P. Perna, J. Camarero, E. Gnecco, D. Faras, and R. Miranda, Nano Lett. **16**, 2 (2016).
[36] S. Koch, D. Stradi, E. Gnecco, S. Barja, S. Kawai, C. Daz, M. Alcam, F. Martn, A. L. Vzquez de Parga, R. Miranda, T. Glatzel, and E. Meyer, ACS Nano **7**, 2927 (2013).
[37] B. Borca, S. Barja, M. Garnica, M. Minniti, A. Politano, J. M. Rodriguez-Garca, J. J. Hinarejos, D. Faras, A. L. V. de Parga, and R. Miranda, New J. Phys. **12**, 093018 (2010).
[38] H. Zhang, C.-X. Liu, X.-L. Qi, X. Dai, Z. Fang, and S.-C. Zhang, Nat. Phys. **5**, 438 (2009).
[39] D. Kong, J. J. Cha, K. Lai, H. Peng, J. G. Analytis, S. Meister, Y. Chen, H.-J. Zhang, I. R. Fisher, Z.-X. Shen, and Y. Cui, ACS Nano **5**, 4698 (2011).
[40] H. Ibach and D. Mills, *Electron Energy Loss Spectroscopy and Surface Vibrations* (Elsevier Science, New York, 2013).
[41] L. V. Min and S.-C. Zhang, Int. J. Mod. Phys. B **27**, 1350177 (2013).

[42] J. Zhou, H.-R. Chang, and D. Xiao, Phys. Rev. B **91**, 035114 (2015).
[43] A. Thakur, R. Sachdeva, and A. Agarwal, J. Phys. Condens. Matter **29**, 105701 (2017).
[44] A. Thakur, K. Sadhukhan, and A. Agarwal, Phys. Rev. B **97**, 035403 (2018).
[45] J. P. Perdew, K. Burke, and M. Ernzerhof, Phys. Rev. Lett. **77**, 3865 (1996).
[46] P. Giannozzi *et al.*, J. Phys. Condens. Matter **21**, 395502 (2009).
[47] J. Enkovaara *et al.*, J. Phys. Condens. Matter **22**, 253202 (2010).
[48] S. R. Bahn and K. W. Jacobsen, Comput. Sci. Eng. **4**, 56 (2002).
[49] J. J. Mortensen, L. B. Hansen, and K. W. Jacobsen, Phys. Rev. B **71**, 035109 (2005).
[50] B. Ghosh, P. Kumar, A. Thakur, Y. S. Chauhan, S. Bhowmick, and A. Agarwal, Phys. Rev. B **96**, 035422 (2017).
[51] K. Momma and F. Izumi, J. Appl. Crystallogr. **44**, 1272 (2011).
[52] Y. Liao, *Practical Electron Microscopy and Database* (Global Sino, 2006), http://www.globalsino.com/EM/.
[53] A. Politano, V. Formoso, and G. Chiarello, Superlattices Microstruct. **46**, 137 (2009).
[54] A. Politano, V. Formoso, and G. Chiarello, J. Phys. Condens. Matter **25**, 305001 (2013).
[55] A. Politano, V. Formoso, and G. Chiarello, Plasmonics **3**, 165 (2008).
[56] M. Rocca, Surf. Sci. Rep. **22**, 1 (1995).
[57] A. A. Govyadinov, A. Konečná, A. Chuvilin, S. Vélez, I. Dolado, A. Y. Nikitin, S. Lopatin, F. Casanova, L. E. Hueso, J. Aizpurua, and R. Hillenbrand, Nat. Commun. **8**, 95 (2017).
[58] A. Politano, V. Formoso, and G. Chiarello, J. Phys. Condens. Matter **25**, 345303 (2013).
[59] Note that there are also surface plasmons, which for large wave vectors are given by the zeros of $\epsilon_{\text{vacuum}}+\epsilon^{\text{RPA}}(\omega)=0$, where ϵ_{vacuum} is the static dielectric constant of vacuum—the surrounding medium. However, in this Letter, we are focused on the bulk 3D plasmon modes only. See Sec. S9 of SM [22] for more details.
[60] T. Low, R. Roldán, H. Wang, F. Xia, P. Avouris, L. M. Moreno, and F. Guinea, Phys. Rev. Lett. **113**, 106802 (2014).
[61] K. Sadhukhan and A. Agarwal, Phys. Rev. B **96**, 035410 (2017).
[62] R. Sachdeva, A. Thakur, G. Vignale, and A. Agarwal, Phys. Rev. B **91**, 205426 (2015).
[63] For the sake of completeness, we point out that a direct comparison between experimental and theoretical loss function for a selected value of the wave vector is unfeasible since the wave vector in the experimental spectra are correlated with loss energies with distinct loss energies corresponding to different momenta.
[64] H. Yi *et al.*, Sci. Rep. **4**, 6106 (2014).